

Accepted Manuscript

Title: Friction Stir Welding of High Density Polyethylene – Carbon Black Composite

Authors: J.Y. Sheikh-Ahmad, Dima S. Ali, Suleyman Deveci, Fahad Almaskari, Firas Jarrar



PII: S0924-0136(18)30430-8
DOI: <https://doi.org/10.1016/j.jmatprotec.2018.09.033>
Reference: PROTEC 15947

To appear in: *Journal of Materials Processing Technology*

Received date: 26-4-2018
Revised date: 26-9-2018
Accepted date: 27-9-2018

Please cite this article as: Sheikh-Ahmad JY, Ali DS, Deveci S, Almaskari F, Jarrar F, Friction Stir Welding of High Density Polyethylene – Carbon Black Composite, *Journal of Materials Processing Tech.* (2018), <https://doi.org/10.1016/j.jmatprotec.2018.09.033>

This is a PDF file of an unedited manuscript that has been accepted for publication. As a service to our customers we are providing this early version of the manuscript. The manuscript will undergo copyediting, typesetting, and review of the resulting proof before it is published in its final form. Please note that during the production process errors may be discovered which could affect the content, and all legal disclaimers that apply to the journal pertain.

Friction Stir Welding of High Density Polyethylene – Carbon Black Composite

J. Y. Sheikh-Ahmad ^{1,a}, Dima S. Ali ^a, Suleyman Deveci ^b, Fahad Almaskari ^c, Firas Jarrar ^a

^a Department of Mechanical Engineering, Petroleum Institute, Part of Khalifa University of Science and Technology, PO Box 2533, Abu Dhabi, United Arab Emirates

^b Borouge Pte. Ltd., Innovation Centre, Sas Al Nakhl, 6951, Abu Dhabi, United Arab Emirates

^c Department of Aerospace Engineering, Khalifa University of Science and Technology, Abu Dhabi, United Arab Emirates

¹ Corresponding author: J. Sheikh-Ahmad, Department of Mechanical Engineering, Khalifa University of Science and Technology, SAS Campus, PO Box 2533, Abu Dhabi, United Arab Emirates. jamal.ahmad@ku.ac.ae, +971 2 607 5338

Abstract

This investigation elucidates the important role of process temperatures in the friction stir welding of polymers. Measurements of the material temperatures were performed by means of an infrared camera and embedded thermocouples under the weld line. An inverse heat conduction method was also utilized to determine the temperature distribution in the workpiece numerically. The weld quality was determined in terms of the amount of defects present in the stir zone and the tensile strength of the joint. It was found that considerable melting occurred under the rotating shoulder and on the trailing side of the rotating pin. Movement of the molten material by the rotating tool created macro- and micro-voids in the stir zone. Crystallinity and nano-hardness measurements indicated that crystallinity was higher under the tool shoulder due

to exposure to high temperatures. Tensile strength of the joint was mainly attributed to fusion welding on the top region and hot forging at the root. Decreasing the welding speed and increasing the penetration depth helped improve the weld quality.

Keywords

High density polyethylene; friction stir welding; thermal history; welding defects; crystallinity; microstructure

1 Introduction

Engineering polymers, as compared to metals are characterized by very low melting temperatures and poor thermal conductivities. This makes their joining by friction stir welding more challenging because of heat accumulation and the difficulty in maintaining the material in the solid state. The material flow under the rotating tool and the characteristic zones of the weld nugget are consequently different in polymers than in metals. These fundamental differences have eventually inspired for different tool designs for the friction stir welding of polymers. Material flow during the friction stir welding of polymers was investigated by Simões and Rodrigues (2014) in bead on plate (BOP) welding of PMMA and Zafar et al. (2016) in welding polyethylene. In comparison to metals, it was concluded that the material flow in welding polymers is restricted to the pin region or pin-influence zone. Stirring due to shoulder rotation was absent from the polymeric welds due to localized heating under the shoulder, lack of friction induced deformation and squeezing out of the molten material. The pin-influence zone remained straight and parallel to the pin unlike the case in metals, which indicated the absence of cross

flow from the shoulder-influence zone to the pin-influence zone. Furthermore, a straight boundary at the bottom of the pin indicated the absence of downward vertical flow. The flow of partially melted material coming from the retreating side to the advancing side caused this material to be extruded against the base material, providing better consolidation on the advancing side of the pin. Low heat conduction also caused flow problems in the deeper zones of the weld when the viscoelasticity became insufficient. This in turn led to the formation of defects on the retreating side of the tool, where the tangential flow of the material caused by pin rotation is opposite to the traverse direction of the tool. Morphology of the deformed polymeric material in the pin-influence zone was examined by Kiss and Czigány (2012) and Vijendra and Sharma (2015), and their observations confirmed the material flow model proposed by Simões and Rodrigues (2014). A spherulitic structure was observed in the central part of the weld nugget of friction stir welded polypropylene, with a finer microstructure than the base material, which is believed to be due to the relatively slow cooling rate in this region. A transition zone was observed at the border of the base material and the pin-influence zone. The transition zone was attributed to skin-core structure formation typically observed in injection molding. This implies that the material has undergone solidification from the liquid phase. The morphology and width of the transition zone was influenced by the pin rotation speed. The width of the transition zone reduced with increasing the pin rotation speed. It was also reported that better joint strength was obtained with smaller overall width and less complex morphology of the transition zone (Kiss and Czigány, 2012).

Significant improvement in the joint strength was achieved by redesigning the FSW tool in order to control the material flow and temperatures under the tool. Azarsa and Mostafapour (2014)

used a rotating pin with stationary heated shoe to weld HDPE sheets. They reported that the optimum welding parameters to achieve maximum flexural strength were tool rotational speed of 1400 rpm, tool traverse speed of 25 mm/min and shoulder temperature of 100 °C. At this optimum condition the flexural strength of welded sample was about 96% of the base material strength. Pirizadeh et al. (2014) and Eslami et al. (2015) designed special tools with stationary shoulders and used them to weld polymers without the application of auxiliary heat. It was reported by Pirizadeh et al. (2014) that tensile strength of the weld decreased when the rotational speed was increased. In addition, there was an optimum value for traverse speed to reach the maximum tensile strength. At the optimum conditions the tensile strength of the weld reached 61% of the base material. Eslami et al. (2015) showed that sound lap welding of PE and PP sheets is attainable using a tool made of stationary brass shoulder enclosed in a Teflon fixture. Vijendra and Sharma (2015) utilized an induction heated tool to FSW 5mm thick HDPE plates. It was shown that joint efficiency of 100% could be obtained at pin rotation speed of 2000 rpm and pin temperature of 45 °C. It was suggested that this high efficiency was attained by good material mixing and the achievement of high level of crystallinity due to the high mixing temperatures. Inaniwa et al. (2013) investigated the weldability of thermoplastics of different flow viscosities. It was determined that sound welding conditions depend on the melt viscosity. Materials with low weld viscosity would have better material flow and better weldability at lower heat inputs (i.e. lower rotational speeds and higher transverse speeds.) Temperature measurements in the weld zone indicated that the maximum material temperature was below the melting temperature for each polymer, which confirms welding in the solid state. Hoseinlathab et al. (2015) studied the effects of rotational speed, traverse speed, geometry, and tilt angle of the tool on the quality and creep behavior of friction stir welded HDPE plates. They reported that tools with cylindrical

pin geometry are preferred in comparison to conical pins. It was also observed that the pin geometry is relatively independent of the welding parameters. The most important welding parameters as determined by this study were rotational speed and traverse speed. Yan et al. (2017) used a double-pin tool for lap welding of high density polyethylene. They showed that joint strength is improved by increasing the rotation speed and decreasing the welding speed. However, the maximum joint efficiency reported was 66.5%, where joint efficiency is defined as the ratio of the joint strength to the base-material strength.

It can be concluded from the literature review above that a great range of welding efficiencies could be obtained by friction stir welding of thermoplastic polymers, and that this variation in welding quality could be closely attributed to the material temperature and state. Inaniwa et al. (2013) and Hoseinlhab (2015) maintained the material largely at the solid state and obtained low weld efficiencies. On the other hand, studies which used higher process temperatures, either by introducing auxiliary heat or by higher rotational speeds, demonstrated that better results are obtained when the material is welded at the liquid state (Bozkurt, 2012; Azarsa and Mostafapour, 2014; Vijendra and Sharma, 2015). Undoubtedly, the process temperatures play a significant role in determining weld quality because the material viscous flow behavior is strain rate and temperature dependent. In this study we look closely at the thermal aspects in friction stir welding of a commercially available HDPE-carbon black composite. Special techniques for measuring the welding temperature are installed and the effects of welding speed, pin rotation speed, and penetration depth on welding temperatures, downforce, and welding quality are investigated. In addition, an inverse heat conduction technique was utilized to investigate the temperature distribution in the weld region.

2 Materials and Methods

2.1 Experimental work

Linear FSW experiments were performed on a manual vertical milling machine. This allowed for the butt welding of two HDPE plates under different conditions of rotational speed, welding speeds and tool penetration. The welding temperatures and forces were measured using thermocouples, an infrared camera, and a force dynamometer, respectively. The experimental setup is shown in figure 1 illustrating the placement of the infrared camera and the force dynamometer relative to the welding area.

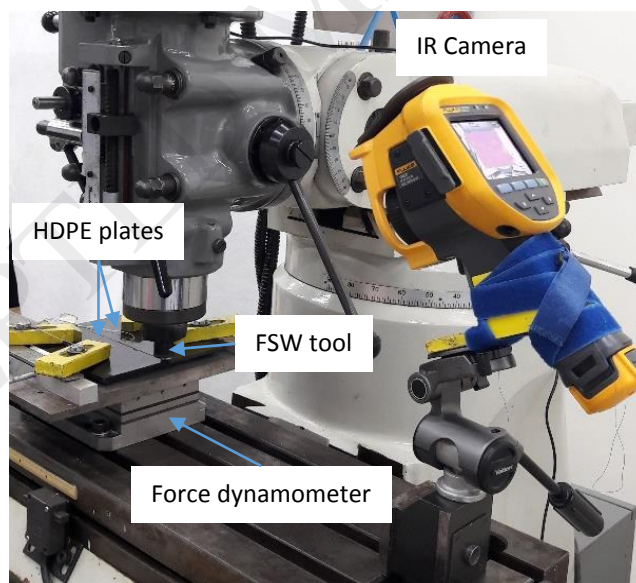


Figure 1. Experimental Setup.

The material used in this study is an HDPE-carbon black composite. The HDPE is a butane/1-hexene copolymer with high molecular weight and wide molecular weight distribution. The

polymer had a crystallinity of approximately 67% and contained 2.3% wt. carbon black with an average particle size of 20nm, which is added for improving resistance to UV light (Deveci et al, 2018). Having a wide molecular weight range causes the material to have a wide range of lamella thickness and melting temperatures (Fawaz et al, 2016). The melting of the shortest polymer chains can start at as low as 50-60 °C. The highest melting point is 131.4 °C (which is also defined as the melting temperature of the material). The material was compression molded to 4.9mm thick flat plaques 180 °C and 5MPa using a frame mould and crystallized from the melt with a cooling rate of 15°C/min according to ISO 293. The plates were later cut into smaller blanks with the dimensions of 160x75 mm², which were used for butt welding along the long side. Table 1 lists the room temperature physical and mechanical properties of the HDPE used in this study.

Table 1. Nominal Physical and Mechanical Properties of HDPE (Source: Borouge Pte. Ltd.)

Density (kg/m ³)	Glass Transition Temp (°C)	Melting Temp (°C)	Yield Strength (MPa)	Thermal Conductivity (W/m.°K)	Specific Heat (J/g.°K)
959	-120	131.4	25	0.28	2.25

The welding tool was made from carbon steel and it has a shoulder diameter of 20 mm and a plain cylindrical pin with a diameter of 6 mm and a height of 4.0 mm. A 1mm deep circular groove was machined on the shoulder surface to improve material retention under the spinning shoulder (figure 2). The welding parameters (rotation speed, traverse speed, and penetration depth) were varied according to a general factorial design as shown in Table 2. The tool rotation was clockwise, and it traversed from right to left as shown in figure 1. Each welding experiment was repeated two times according to the design of experiments (DOE). The ranges of the process parameters and pin geometry were selected based on recommendations found in the works of

Inaniwa et al. (2013), Azarsa and Mostafapour (2014), Hoseinlaghab et al, (2015), and on the results of some screening tests performed in the lab. The tilt angle was maintained at 1° for all experiments. According to the works of Bozkurt (2012) and Hoseinlaghab et al. (2015), the tilt angle had very little influence on weld quality in FSW of HDPE. The screening tests indicated that a tilt of 1° helped reduce flashing.

Table 2. Design of Experiment.

Factors	Levels		
	1	2	3
Rotation speed (rpm)	800	1000	1200
Traverse speed (mm/min)	20	30	40
Plunge depth (mm)	4.1	4.2	

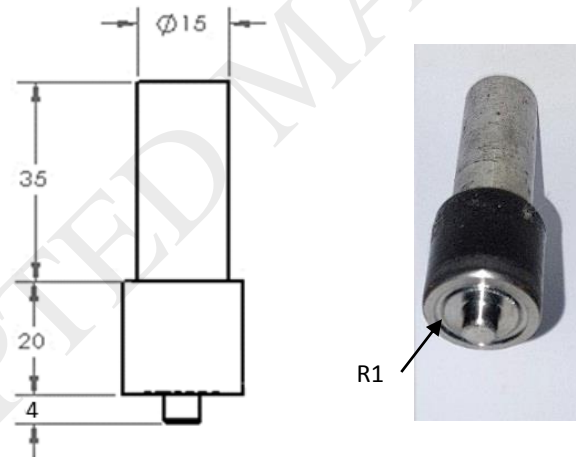


Figure 2. FSW tool geometry.

Temperature measurements were done both at the top and bottom of the abutted plates. The temperatures at the bottom surface of the weld line were measured by placing three type K thermocouples underneath the HDPE plates inserted through shallow grooves in the mantle. Thermocouples with gage wire 30 were used for maximum response speed. At the top of the plate the temperature was measured using a Fluke Ti400 infrared camera mounted on the

machine table such that the pin and the weld line are always in the focused field of view. An image was recorded by the camera every 10 seconds and SmartView software was later used to read the temperature field of interest. The downforce and the feed force during the plunging and welding stages were measured by a Kistler Type 9257B force dynamometer which was fixed under the mantle. The depth of the tool penetration into the material during the plunging stage was controlled by the means of a digital dial indicator that displayed the penetration depth of the pin.

After welding tensile test specimens were cut perpendicular to the weld line using a CNC router. Two specimens were cut for each welded plate according to ISO 5427-2/1B tensile test specimen. The total sample length was 150mm, and the gage length and width were 50mm and 10mm, respectively. An optical microscope was used to inspect the weld quality visually by observing the cross sections of the weld line of the tensile specimens. Weld defects such as voids and tunnels were identified and photographed. The total cross sectional area of voids was evaluated using an image measuring software. After the optical inspection, the samples were tensile tested on a Zwick Z010 system at room temperature and a cross-head speed of 50mm/min. For inspection of the macrostructure and microstructure of the weld region, 50 micron of slices were removed from the cross-section of the weld by using a sliding microtome (Thermo Fisher HM450) for microscopic analyses. Finally, analysis of the results was performed with Minitab statistical analysis software.

2.2 Numerical simulation of heat conduction

The heat conduction problem into the workpiece was simulated numerically using Abaqus/Explicit as shown in figure 3. The numerical model for the workpiece consisted of a rectangular prism of dimensions $100 \times 40 \times 5 \text{ mm}^3$ as shown. The heat from friction under the tool shoulder and by the stirring action of the pin was modeled as moving heat sources. A linearly distributed surface heat source, \dot{q}_s , was used to represent the frictional heat under the tool shoulder with a maximum value at the outer diameter. A body heat source, \dot{q}_b , was used to represent heat generated by the stirring action of the pin. Both heat sources were traversed along the weld line at constant welding speed v using DFLUX user subroutine. The boundary conditions on the different surfaces of the workpiece are also shown on figure 3. Heat loss by convection to air and by conduction to the mantle were assumed on the top and bottom surfaces of the HDPE plate, respectively and different heat transfer coefficients were used on these surfaces. All other surfaces were assumed to be insulated. The convection heat transfer coefficient value for free convection ranges from 10 to $200 \text{ W/m}^2\text{-K}$ (Whielaw, 2018). In the present work the approximate values for h were determined by trial and error with the objective of minimizing the difference between the experimental measurements and the simulated temperatures. The heat transfer coefficient on the bottom surface (h_2) was set higher than the top surface (h_1) because the bottom surface was in contact with the cold mantle. The heat transfer coefficients used in the current simulation were $h_1 = 30 \text{ W/}^\circ\text{K.m}^2$ and $h_2 = 60 \text{ W/}^\circ\text{K.m}^2$. It is worth noting here that variations in the values of h did not greatly affect the overall solution of the problem. This observation was also reported by Kim et al. (2006). Temperature dependent thermal properties of the workpiece were taken from the work of Santos et al. (2013) and are shown in Table (3). The element type used for the workpiece was DC3D8 (thermal analysis), a

3D 8-noded linear heat transfer brick type element. 24000 elements of size $1 \times 1 \times 0.9 \text{ mm}^3$ and 28987 nodes were used. This size of the mesh provided a good compromise between accuracy and computational time. It was determined by mesh sensitivity analysis that the next mesh size of $0.5 \times 0.5 \times 0.5 \text{ mm}^3$ provided only 0.8% improvement in prediction accuracy at the expense of more than 1000% increase in computational time.

Inverse heat conduction method was used to determine the amount of surface and body heat fluxes going into the workpiece. In an inverse method, the heat flux applied is systematically adjusted until the boundary temperatures determined by the numerical solution are matched to those measured by experiment. The heat diffusion problem in the workpiece is 3-D nonlinear, transient as represented by the heat conduction equation:

$$\nabla \cdot k \nabla T + Q = \rho c \frac{\partial T}{\partial t} \quad (1)$$

where k is thermal conductivity, T is temperature, Q is internal heat source, ρ is density, c is specific heat and t is time. Equation (1) is subject to the boundary conditions:

$-k_{\eta}(T) \frac{\partial T}{\partial z} = h_i(T - T_{\infty})$ on top surface and bottom surfaces, where h_1 and h_2 are the heat transfer coefficients for top and bottom surfaces, respectively and T_{∞} is ambient temperature,

$-k(T) \frac{\partial T}{\partial z}(x, y, z_o, t) = \dot{q}_s$ on the top surface, where \dot{q}_s is the amount of moving heat flux generated by shoulder friction and conducted into the workpiece,

$-k_{\eta}(T) \frac{\partial T}{\partial \eta} = 0$ on the remaining surfaces, and having the initial condition:

$T(x, y, z, t) = T_o$, at $t = 0$.

The magnitude of each heat flux was determined by minimizing the objective functions in equations (2) and (3) over time and space domains, respectively:

$$SSE1 = \sum_{i=1}^n \sum_{t=1}^m (Y_i(t) - T_i(t))^2 \quad (2)$$

$$SSE2 = \sum_{j=1}^l \sum_{x=1}^k (Y_j(y) - T_j(y))^2 \quad (3)$$

where SSE1 and SSE2 are sum of square errors in time and space domains, respectively, Y_i is measured temperature history and T_i is simulation temperature history for thermocouple location i under the weld line and Y_j is the measured temperature and T_j is the simulated temperature at location y along line AB on the top surface of the workpiece just behind the tool shoulder (figure 3).

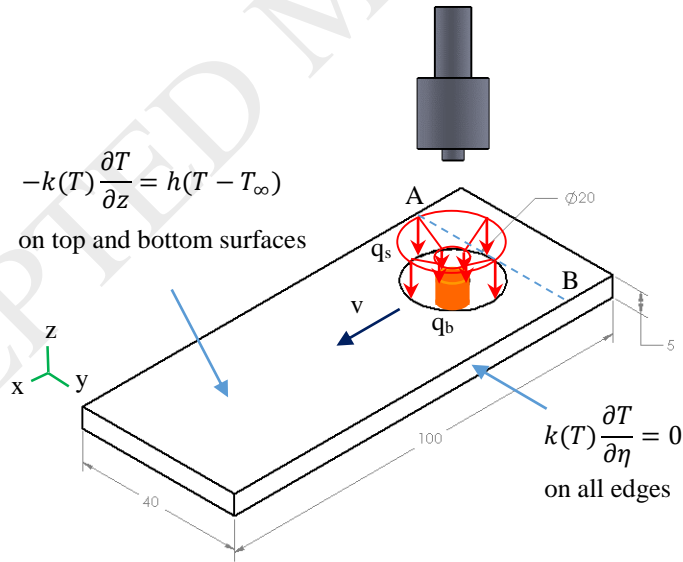


Figure 3. Numerical of workpiece with body and surface moving heat sources.

Table 3. Material properties of HDEP (Santos et al., 2013)

Temperature (°C)	Thermal conductivity (W/m.K)	Temperature (°C)	Average Heat Capacity J/(g·K)
24	0.55	34	1.882
70	0.42	98	2.554
115	0.4	110	3.226
133	2.27	118	4.032
150	0.22	121	5.376
		124	7.661
		132	24.462
		140	2.419

3 Results and Discussion

3.1 Weld morphology

The external appearance of the weld line was closely related to the state of the material under the tool shoulder. When the material was solid at relatively low temperatures, the weld line appeared to be of uniform width and had clear striations indicating the tracks left by the tool shoulder, similar to weld appearances in metals. As the material temperature reached the melting point, the weld line became irregular and of nonuniform width. Figure 4(a) shows the weld line at relatively high temperatures and high downward force. The surface appearance of the weld is characterized by striations of different depths, indicating the frequent sinking of the tool shoulder into the softened material. Figure 4(b) shows a typical weld line appearance with a clear indication that melting and solidification of the material under the shoulder has occurred, as indicated by the shiny surface of the weld line. Depressions along the weld line indicate the collapse of the material in the weld zone due to loss of volume by ejection and/or by shrinkage. Figure 4(c) shows that a groove formed along the weld line when the softened material was pushed ahead of the pin. The tendency to form grooves decreased with the increase in the

rotation speed and the corresponding increase in welding temperatures. The nonuniform appearance of the weld line in figure 4(b) implies nonuniformity of the structure of the material in the weld zone below the surface of the weld. As shown below, the welding process of the HDPE was rather unstable with intermittent formation of defects such as voids and wormholes which were buried under the surface. The surface morphology in figure 4(b) may indicate the presence of such defects in the left half of the welded plates. Such defects are shown in figures 5 and 6.

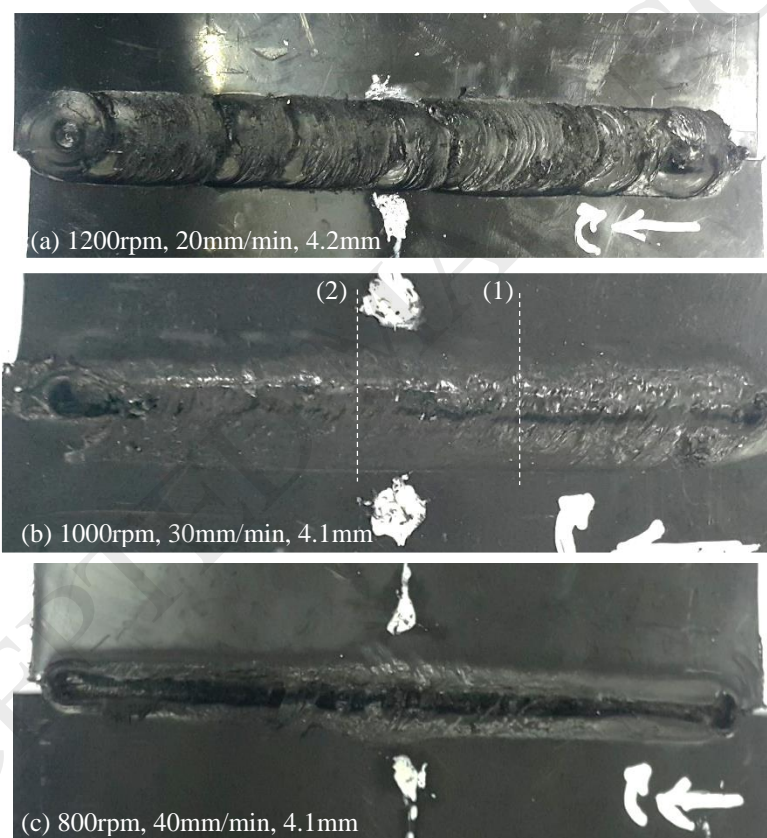


Figure 4. Weld line appearances (a) uniform with striations, (b) uniform with surface melting, and (c) groove. Welding conditions are as indicated.

Figure 5(a) shows the microtomed cross sections of the weld line in figure 4(b) at location (1) as indicated on the figure, with a schematic of the friction stir welding tool imposed on the image and the advancing side placed on the left. Thinning of the cross section at the weld line is evident

as indicated by the gap between the tool shoulder and the surface of the weld. The amount of thinning varied along the weld line and was less severe at location (2). Almost all welding conditions in this study have caused thinning to some extent, apparently due to ejection of the softened and/or melted material by the rotating shoulder. However, it was more profound at the rotational speed of 1200 rpm and welding speed of 30 mm/min due to the high temperatures. The weld nugget and material flow lines in the stir zone are clearly visible in figure 5(a), with material clearly being displaced toward the advancing side. The weld nugget (pin-influence zone) is perfectly rectangular with straight sides and straight bottom, indicating that material flow was restricted to this zone and that both horizontal and vertical cross flow were absent. Figures 5(b) and 5(c) show high magnification images of corners A and B, respectively of the weld nugget as indicated on figure 5(a). The bonding between the material in the stir zone and the base material on the advancing side appears to be sound as shown in figure 5(b). However, the lack of bonding is evident on the retreating side of the stir zone as indicated by arrows on figure 5(c). A similar observation was reported by Simões and Rodrigues (2014) and was attributed to material extrusion on the advancing side and opposite flow directions of pin and traverse speed on the retreating side. Both figures show a distinctive transition zone (TZ) between the stir zone and the base material similar to that reported by Kiss and Czigány (2012) and Vijendra and Sharma (2015). The width of the transition zone was larger on the advancing side than on the retreating side and bottom of the weld. It is also shown in figure 5(a) that the tip of the pin did not reach the bottom of the plates and thus a zone of material that was joined only by forging existed at the bottom of the weld nugget in the form of a root defect.

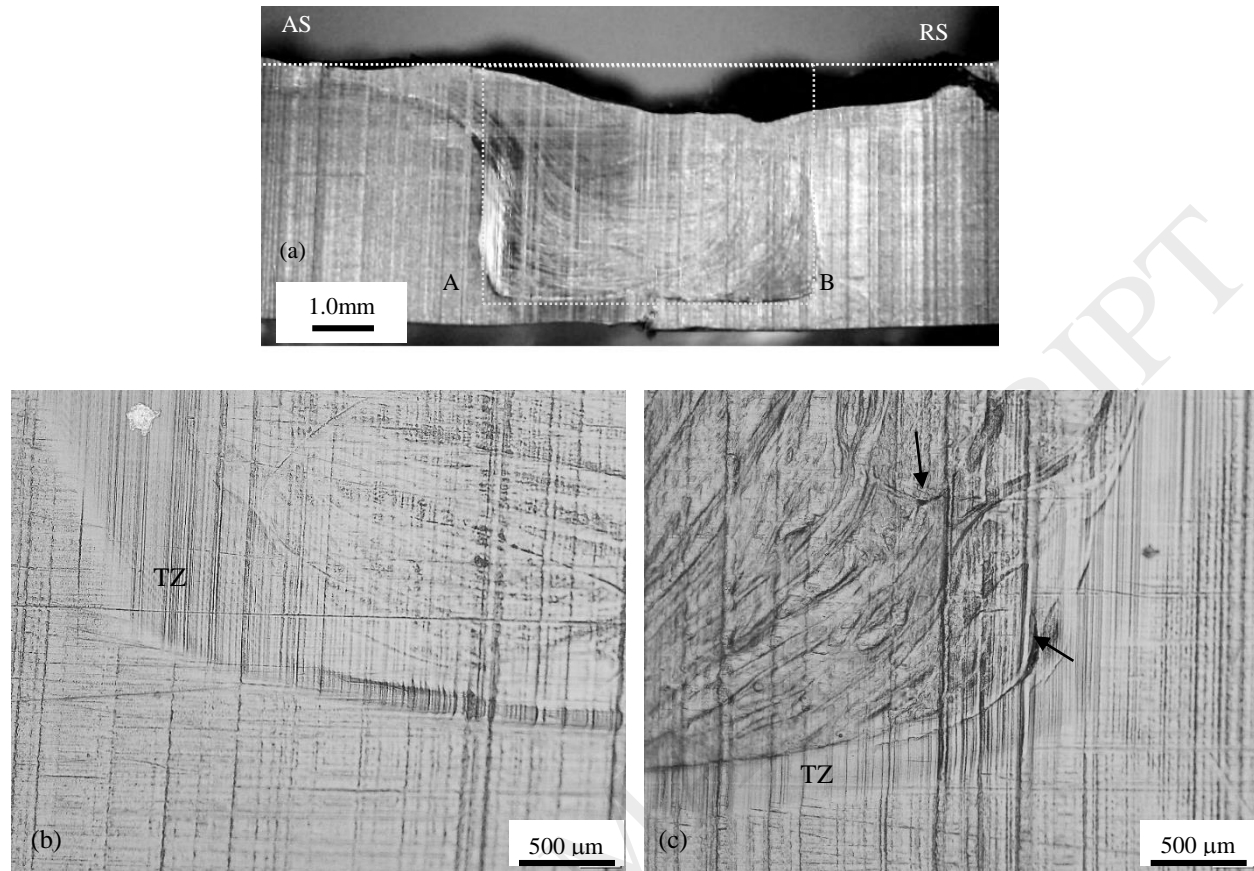


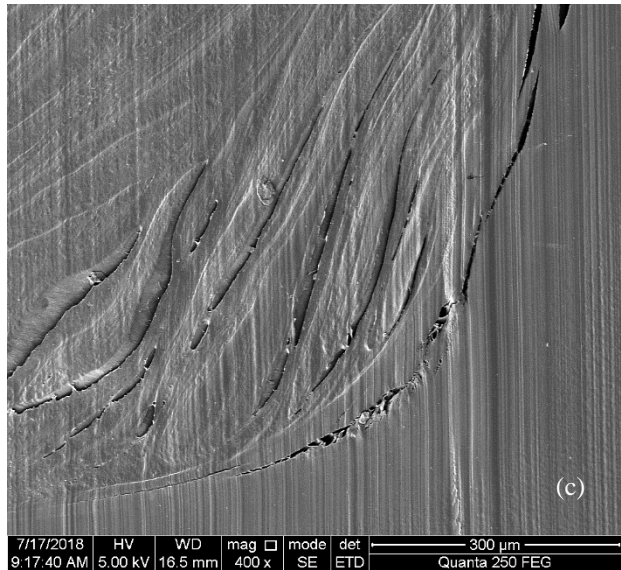
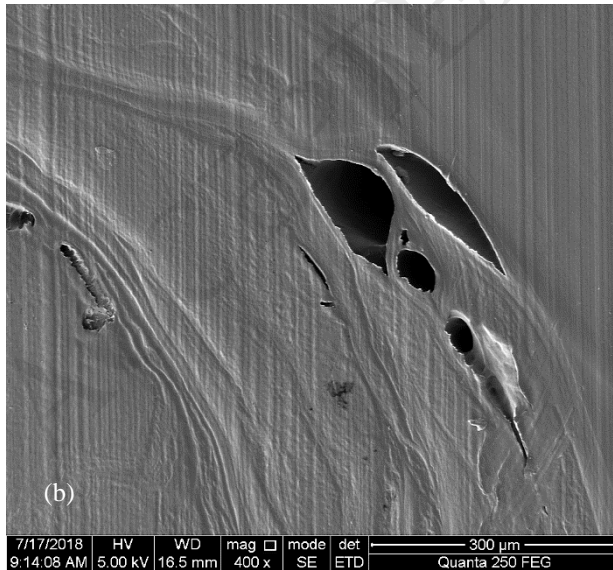
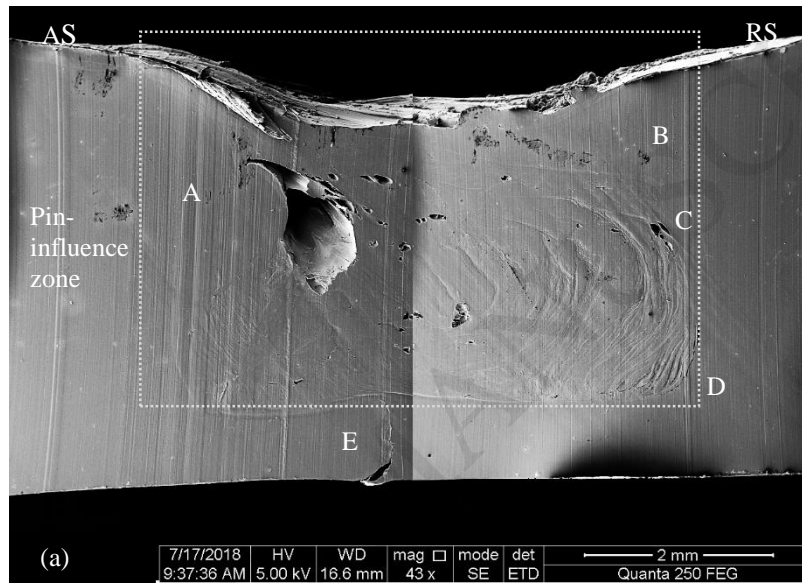
Figure 5. Macrostructures of the cross section of the weld line for condition (1000rpm, 30mm/min, 4.1mm) at location 1 (a), high magnification images at corners A (b) and B (c).

Figure 6(a) shows an SEM image of the microtomed cross section for the weld line at condition (1000rpm, 30mm/min, 4.1mm), shown on figure 4(b) as location (2). The pin-influenced zone is marked on the figure by a dotted rectangle. While the weld nugget at section (1) did not contain any sizable voids (figure 5(a)), the one at section (2) contained a large wormhole as well as smaller voids at the nugget-base material interface. Apparently, the wormhole formed at the beginning of the weld and disappeared later in the second half of the weld line. When a void is continuous along the weld line, it is called a tunnel, but if the void is intermittent, it is called a wormhole. Tunnels and wormholes like this and of various sizes appeared for most welding conditions and they consistently formed on the advancing side of the stir zone. In welding

aluminum alloys, tunnels occur due to the lack of material ductility caused by insufficient heat input. However, in the case of HDPE, the process temperatures are way above the glass transition temperature and often reach the melting point. Therefore, tunnel formation is attributed to severe material displacement and ejection outside the stir zone. Tunnels and voids may also form due to shrinkage upon solidification as the material cools down. When the tunnel is large enough to reach the surface of the weld, a groove is formed as shown in figure 4(c). At 4.1 mm plunge depth, groove defects were associated mostly with pin rotational speeds of 800 and 1000 rpm and welding speed of 40 mm/min. Grooves also became more frequent at the higher penetration depth of 4.2 mm.

Different material regions can be clearly identified in the pin-influence zone as marked by letters A to C on figure 6(a). Regions A and B show material with no visible flow lines and no visible boundary with the base material. The material in this zone must have undergone melting and solidification, resulting in complete fusion with the base material. The large amount of voids on the top left quarter of the pin-influence zone suggests the possibility of melting and material ejection outside the pin-influence zone. Different types of voids appear on the bottom half of the pin-influence zone. Figure 6(b) shows the interface between the stir zone and the parent material on the retreating side at location C on figure 6(a). The voids at this location appear to be subjected to mode I loading (opening). Figure 6(c) shows the voids at location D, which are of different type than those at location C. These voids are longer, aligned with the flow lines and appear to be loaded in mode II (shear). These types of voids and their loading is consistent with the material loading at the retreating side represented by opposing directions of pin rotation speed and transverse speed (shear). Figure 6(d) shows the area under the pin-influence zone at

location E (root defect). The material in this region appear to be joined together by the pin pressure, however, the joint has several cracks along its length indicating insufficient bonding. A transition zone between the pin-influence zone and the base material is clearly visible at the top of the figure. The thickness of the transition zone at this location is approximately 100 μm .



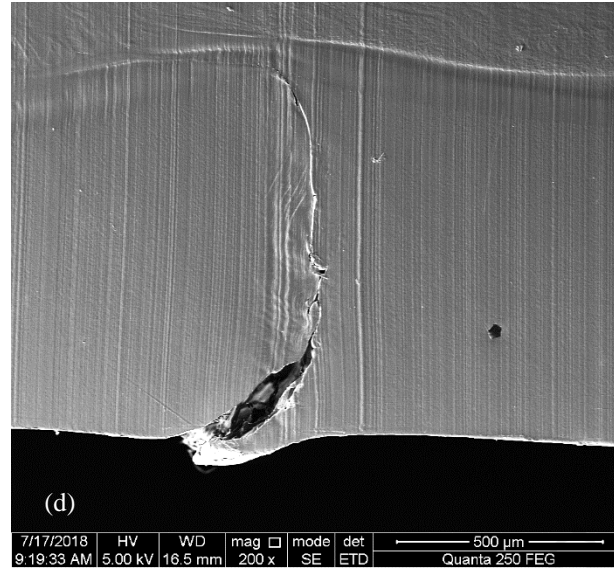


Figure 6. SEM images of the cross section of friction stir welded joint at conditions 1000rpm rotation speed, 30mm/min traverse speed and 4.1mm plunge depth (a), details of voids at location C (b), details of voids at location D (c), root defect at location E (d).

3.2 Thermal history

The temperature field on the top surface of the welded HDPE plates was recorded by the infrared camera at the rate of one frame every 10 seconds. Figure 7 shows an example thermal image at the welding condition of 800 rpm, 20 mm/min and 4.2mm penetration depth. This image was recorded when the tool was approximately halfway along the weld line. The temperature distribution along the line AB just behind the shoulder of the tool is also imposed on the image. It is shown that the temperature across the weld line rises sharply in a short distance due to material heating from friction. Heat conduction to both sides of the weld is very small due to poor thermal conductivity. Furthermore, the temperature profile is almost symmetric with respect to the weld line with a maximum temperature of about 130 °C, which is close to the maximum melting temperature for this polymer. Symmetric temperature distribution across the weld line was also suggested by Simões and Rodrigues (2014) based on microstructural analysis of the weld cross section. The maximum weld line temperatures for all the welding combinations were

determined using the same procedure explained above. It was found that the maximum weld line temperature on the top surface rises slowly during dwell time at the beginning of the weld and then reaches a steady state with increasing welding time for most welding conditions. The steady state maximum weld line temperature was found to be approximately in the range from 120 to 140 °C and did not seem to vary significantly with welding parameters. This indicates that partial or complete melting of the material under the shoulder has occurred for all welding conditions.

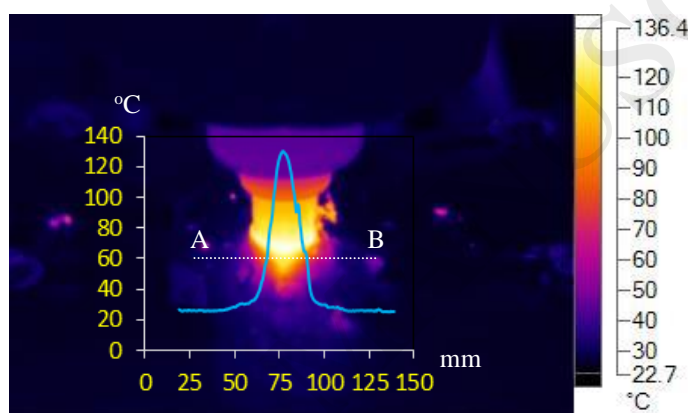


Figure 7. Temperature field on the top surface of the HDPE sheets for welding condition of 800 rpm, 20 mm/min and 4.2mm penetration depth. Trace shows temperatures along line AB just behind the tool shoulder with the advancing side on the left of the image.

Thermal history at the bottom of the welds was recorded using three thermocouples placed at different locations along the weld line, namely near beginning of the weld, at the middle and near the end of the weld. Figure 8 shows a typical thermal history plot recorded during the tool traverse along the weld line. Thermocouple 4 (T4) measured the temperature at the beginning of the weld, thermocouple 2 (T2) at the middle, and thermocouple 5 (T5) near the end of the weld. The temperature at each point rises up suddenly as the rotating pin passes over the thermocouple bead and then decreases slowly as the pin moves away and the material cools down. The three thermocouples recorded temperature peaks ranging from 42 to 45 °C. An average under-weld

peak temperature was calculated from the three thermocouples for each experiment and the results were analyzed as discussed in section 3.8.

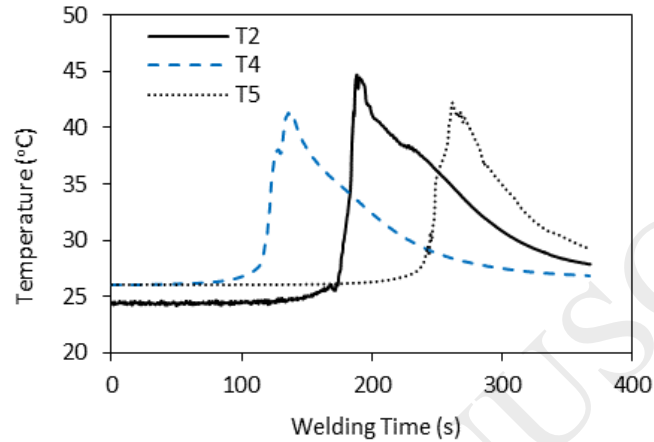


Figure 8. Thermal history for under weld thermocouples for weld conditions (800rpm, 30mm/min, 4.1mm.)

3.3 Simulation results of the heat conduction problem

Surface and under-weld temperature measurements discussed above indicate the occurrence of a steep gradient in the material temperatures from top to bottom, where temperatures on the top are in the melting range while temperatures at the bottom of the weld are relatively cold. This steep gradient is mainly due to poor heat diffusion by conduction through the thickness and the lack of vertical material flow in the pin-influenced zone. Controlling the temperature in the weld zone is a vital part of executing FSW of polymeric materials. According to Muñoz (2015), material over fluidity due to melting contributes many flaws. As the material is melting, it loses its viscosity and over flows out of the welding zone. On the other hand, Bozkurt (2012) reported that the lack of proper heat diffusion to the bottom parts of the weld contributes to a decrease in tensile strength as a result of root defects. To better understand the heat distribution in the welding zone,

an inverse heat conduction problem was utilized to simulate the thermal aspect of FSW, as a first approximation. Results of this analysis are shown in figures 9 and 10.

Figure 9 shows the temperature distribution on the top surface of the workpiece as a result of moving surface and body heat sources \dot{q}_s and \dot{q}_b of magnitudes 73 mW/mm^2 and 15 mW/mm^3 , respectively. These magnitudes of heat fluxes were determined by optimizing the objective functions in equations (2) and (3) with respect to the measured temperatures along line AB on the top surface (as shown in figure 7) and thermal histories of three thermocouples on the bottom surface (as shown in figure 8). It can be seen that the material temperatures under the tool shoulder are relatively high as compared to those in the stirring zone and away from the tool shoulder. The highest surface temperatures occur on the trailing side of the tool shoulder due to the effect of heat accumulation. Furthermore, the temperature distribution on the surface seems to be symmetric with respect to the weld line due to the absence of material movement by stirring in the thermal model.

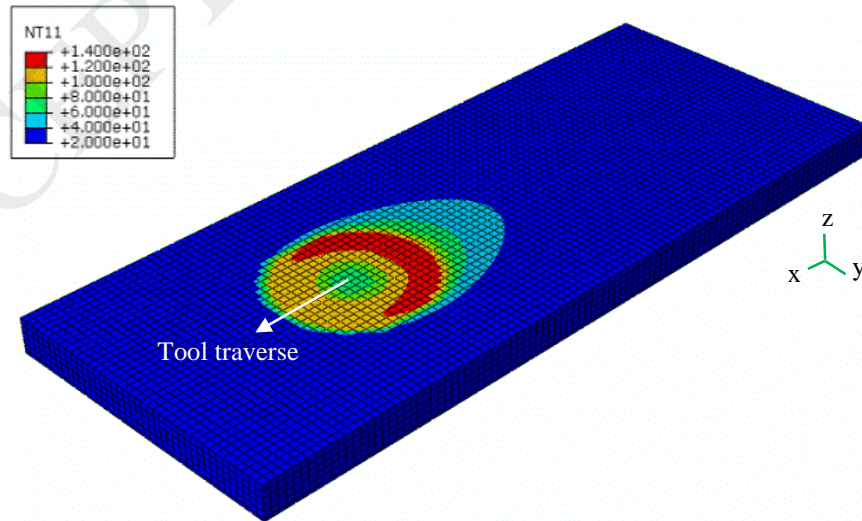


Figure 9. Temperature distribution on the top surface of workpiece for welding speed of 30 mm/min.

Figure 10(a) shows the temperature distribution on a transverse cross section passing through the center of the pin. Figure 10(b) shows the temperature distribution on a longitudinal cross section at the middle of the workpiece. A schematic of the FSW tool is imposed on each image to clarify the different welding zones. It is apparent that the temperatures under the shoulder are higher than the other regions of the weld zone with temperatures in the range from 100 to 133°C in a 1 mm deep zone below the shoulder. Heat accumulation under the trailing end of the shoulder is more profound and reaches a depth of almost 2mm (figure 10(b)). The material at the leading end of the tool shoulder is cooler and the depth of heat penetration is much less than 1mm. Since this material is not transferred to the pin-influence zone by cross flow, it is ejected outside the weld zone by the centrifugal force of the shoulder. This explains the gap between the shoulder and the material as shown in figures 5(a) and 6(a). The temperatures in the pin-influence zone vary greatly from the trailing side of the pin to the leading side and from top to bottom, with significant melting occurring at the top part of the trailing side as shown in figure 10(b). Conceivably, this molten material is moved by the pin rotation to the advancing side and then partly ejected from the stir zone, leading to the formation of large voids in the form of tunnels and wormholes as shown in figure 6(a).

Temperature histories of the material at several locations on the cross section of the weld are plotted in figure 11. These locations are shown on figure 10(a) and they are on the top surface at the center of the pin (A), the advancing side of the pin-influenced zone (B) and approximately halfway under the shoulder (C). Three other locations, D, E and F are at the same radial positions as A, B and C, but 1.8 mm below the surface. Location G is at the weld line on the bottom surface and it corresponds to thermocouple locations TC1, TC2 and TC3. The temperature

histories at A, B and D show that the material is subjected to two heating cycles caused by the moving heat sources at the leading edge and the trailing edge of the shoulder. It can be seen that the first heating cycle is of lower temperatures than the second. The heating cycles for the material at point C, which is always under the shoulder, are less profound and are fused together because of the continuous exposure to frictional heat. The peak temperatures at these locations are well in the melting temperature range of HDPE. The minimum temperature is also in the melting range for points B, C and D. The minimum temperature for point A at the center of the tool drops below the melting point, and hence, melting and solidification occur for this material over the time of the thermal cycle. The remaining points F, E and G are subjected to temperatures below the melting point. Therefore, material flow and mixing is limited at these locations.

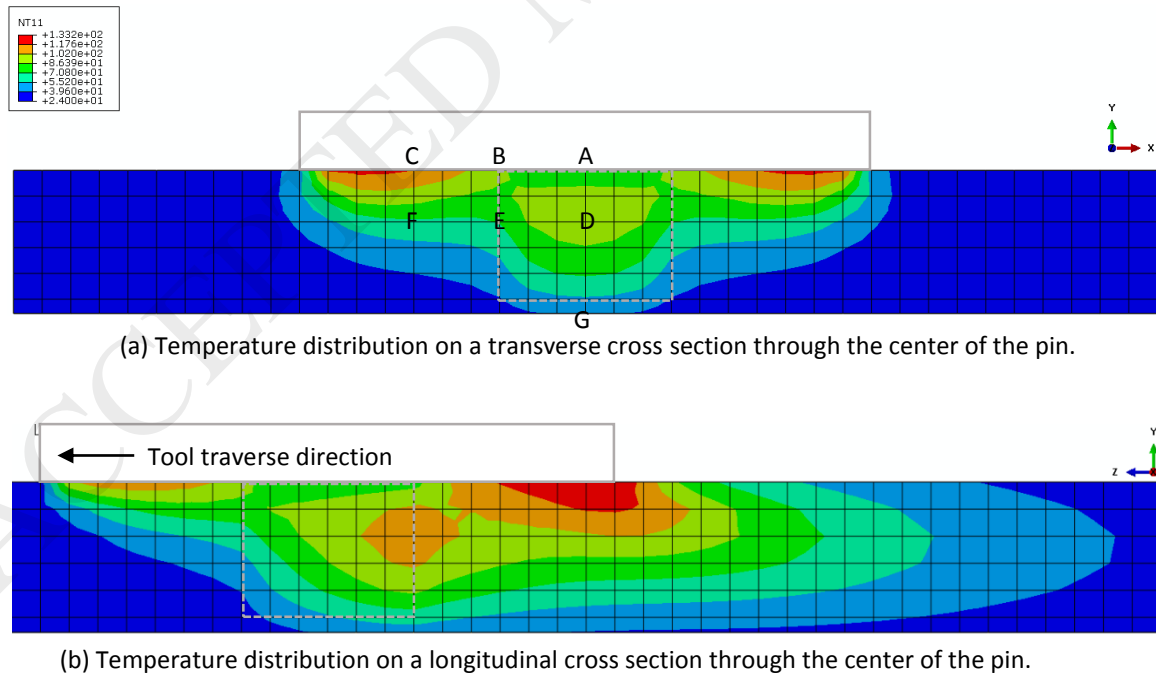


Figure 10. Simulated temperature distributions in the material for welding speed of 30 mm/min.

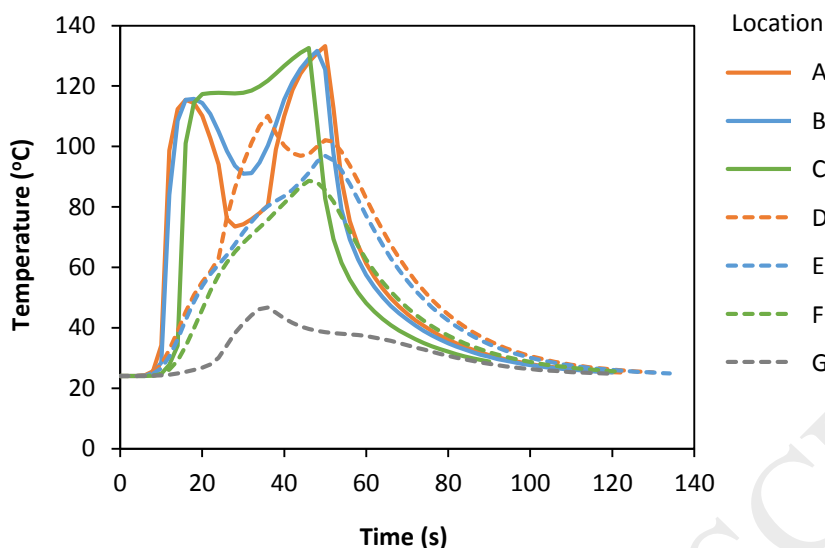


Figure 11. Simulated temperature histories at locations A to G shown in figure 10(a) for a welding speed of 30 mm/min.

3.4 Joint strength

A typical engineering tensile stress plot of the HDPE composite base material is shown in figure 12(a). This behavior is characteristic of semi-crystalline solid polymers. The graph has two distinct parts, one before the tensile strength at (A), and the other after it. In the first part, the material exhibits uniform deformation in the gage area until the tensile stress of approximately 26 MPa is reached. The engineering strain at this tensile strength was about 7.3%. Necking sets in after this stress and the neck propagates in the gage length under constant stress level (B) due to cold drawing. This is typically associated with stretching and realignment of the molecular chains in the direction of the applied load. The tensile stress at (A) is often referred to as the yield strength of the polymer.

A representative tensile stress behavior of the welded samples is shown in figure 12(b) for rotation speed of 1000 rpm, welding speed of 30 mm/min and penetration depth of 4.1 mm. Run

1 and Run 2 are the two repeats of this combination of parameters, and A and B are the two test samples cut from each run at two different locations across the weld line (middle of the upper part and middle of the lower part of the welded plate). A great variation in the yield strength of the different test samples of the same combination of parameters is shown. This is mainly attributed to the discontinuity and non-uniformity in some of the defects, such as tunnels and voids along the weld line due to the great instability in the welding process. The average yield strength and yield strain for this combination were found to be 16.4 MPa and 1.9%, respectively. Apparently, FSW has resulted in reducing both the yield strength by 37% and the corresponding strain by 74% from the base material due to the presence of weld defects. Examination of the fracture location of the welded samples have shown that they consistently failed on the retreating side. This was anticipated in view of the lack of bonding which was present on the retreating side of the pin-influenced zone as shown in figure 6. Similar observations were also reported by Inaniwa et al. (2013), Simões and Rodrigues (2014) and Vijendra and Sharma (2015).

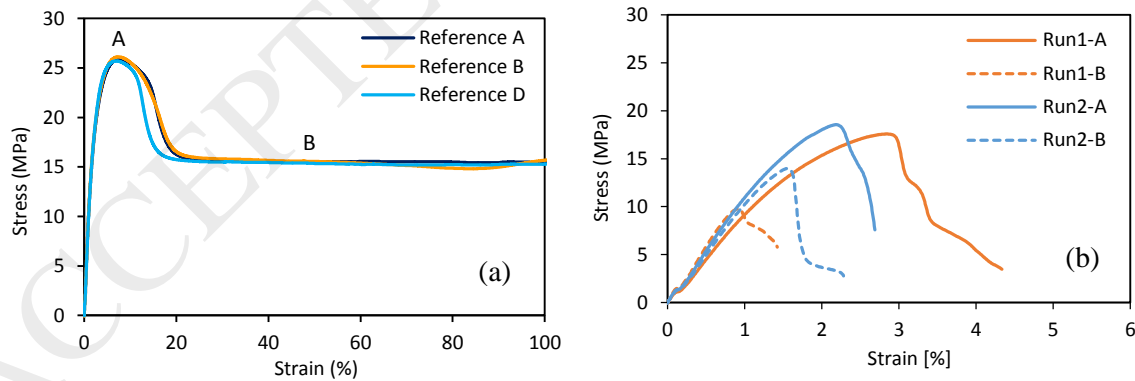


Figure 12. Typical tensile test performance of the base material for three reference samples (a) and the welded material (b). Welding conditions: 1000rpm, 30mm/min, 4.1mm depth.

3.5 Fracture morphology

Fracture surfaces of the tensile samples were inspected inside the scanning electron microscope. SEM images of the fracture surfaces of two samples, one demonstrating low yield strength of 4 MPa (sample 1) and the other demonstrating high yield strength of 16 MPa (sample 2) are shown in figures 13 and 14, respectively. The fracture surface of sample 1 shows a flat brittle like area at the bottom root region below the pin-influence zone. This is attributed to the lack of fusion between the two abutting plates at the root of the weld, caused by relatively low material temperatures and low pressure. The middle part of the fracture surface shows the appearance of a mixed material without fibrillation and lack of mechanical deformation, which can be attributed to insufficient mechanical mixing at relatively low temperatures. Apparently at this area, material was not welded at all and it did not contribute to the tensile strength of the sample. The upper part of the image shows limited ductility with minor fibrillations which contributed to the measured tensile strength of the sample. The material in this area was welded by fusion due to melting and solidification.

The SEM image of the fracture surface of sample 2 shows ductile deformation at the bottom (root area) which is different from sample 1 and is indicative of a good root weld obtained by forging at high temperatures obtained at the higher penetration depth as discussed in section 3.8. A large amount of material deformation is visible at this part together with cavities most probably inherent from the welding process and enlarged during elongation. Unlike sample 1, mechanical deformation of this bottom area must have contributed to the tensile strength of the sample. Similar to sample 1, sample 2 also shows a mixed area without any fibrillation although the volume of insufficient mixing area is less than sample 1. At the middle part, appearance of

the material does not show mechanical deformation. Therefore, no contribution to the tensile strength of the sample is expected from this area. Upper part of the fracture surface shows much more elongated fibrils than sample 1, which indicates higher ductility during the tensile tests. Similar to sample 1, the material in this region was welded by fusion due to melting. However, the extent of fusion welding is more in sample 2 than sample 1. In combination with contribution from the bottom root area, the total tensile strength of sample 2 showed higher value than sample 1.

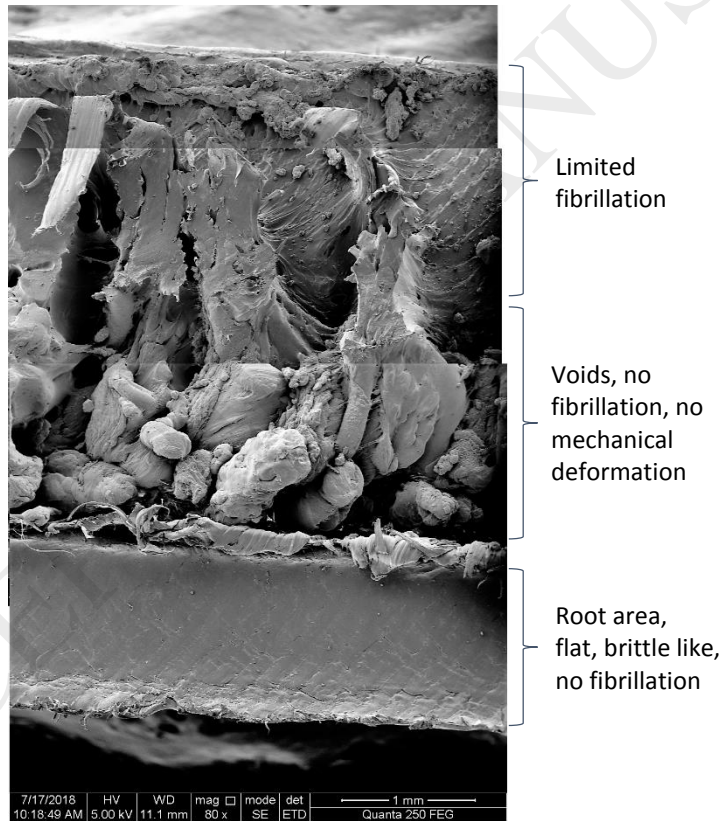


Figure 13. Macrostructure morphology of tensile fracture surface for sample 1 (welding conditions: 800rpm, 20mm/min, 4.1mm depth.)

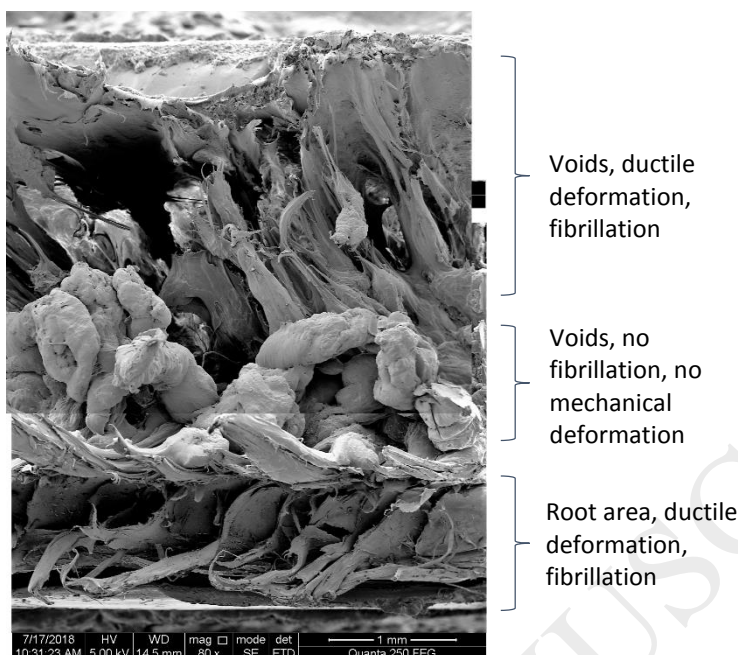


Figure 14. Microstructure morphology of tensile fracture surface for sample 2 (welding conditions: 1000rpm, 40mm/min, 4.2mm depth.)

3.6 DSC analysis

Differential scanning calorimetry (DSC) was conducted on an indium and tin calibrated TA instruments Q2000 equipped with RCS90 cooling system. A sample mass of 3 ± 0.2 mg was directly cut from the welded samples and encapsulated in aluminum pans. Ultra-high purity dry nitrogen was used as an inert atmosphere for all tests. The samples were first heated from room temperature to 200 °C at 10 °C/min and held for 5 minutes to erase thermal history. Then the polymer melt was cooled at 10 °C/min to 0 °C and held for 5 minutes. Finally, the sample was heated from 0 °C to 200 °C at 10 °C/min. The enthalpy of fusion was determined from the peak area of the first and the second heating curves between the baseline points at 50 and 140 °C. Similarly, the enthalpy of crystallization was determined from the peak area of the cooling curves between the baseline points at 40 and 125 °C. The degree of crystallinity was computed

from enthalpy of fusion, assuming enthalpy of fusion for 100% crystalline PE is 290 J/g (Mandelkern and Alamo, 2007).

According to the heat transfer simulations given in figures 10 and 11, zones around points A, B and C were exposed to temperatures close to the material melting temperature for a short period of time due to the first and second frictional heating from the leading and trailing edges of the tool shoulder. The temperature drops down significantly in between these two tool contacts for points A and B as shown in figure 11. The temperature decrease between these two tool contacts becomes less as the distance between the center of tool pin and simulation point increases, in the order of A, B and C. In other words, total heating energy absorbed by the material is higher at zones around C than other zones. The effect of such a difference in thermal history on the crystalline structure of the material under the tool pin (Zone A-D) and under the tool shoulder (Zone C-F) was captured with DSC measurements. It was observed that the melting temperature (T_m) and enthalpy of fusion (ΔH_m) at first heating cycle of DSC experiments were higher for samples taken from the Zone C-F than the samples taken from the Zone A-D, whereas such differences almost disappeared after the second heating scan of DSC experiments. This behavior reveals that the material in Zone C-F was exposed to temperatures that are high enough to initiate post crystallization but short enough to prevent any thermo-oxidative degradation (Deveci and Oner, 2015). Crystallinity of the material at zone C-F was found to be higher than that of the material at zone A-D as shown in table 4. Squeo et al. (2009) have shown similar findings based on DSC measurements in the friction zone and outside the friction zone and reported that lower crystallinity levels were obtained in the weld bead due to shearing action of the rotating pin on the polymer crystalline structure. Determining crystallinity by DSC in smaller areas to

understand the microstructure distribution within the welding zone was not possible due to limitations in sampling size. However microstructure changes along the friction stir welding area due to differences in mechanical and thermal history were further investigated by nano indentation tests.

Table 4. DSC results

Sample Description	T_m , 1 st heating (°C)	ΔH_m , 1 st heating (J/g)	Cryst. (%)	T_c , (°C)	ΔH_c , (J/g)	T_m , 2 nd heating (°C)	ΔH_m , 2 nd heating (J/g)
Zone C-F	130.4	204	70	118.3	196	130.1	193
Zone A-D	128.9	195	67	118.6	198	129.9	194

3.7 Nano indentation

Nano indentations tests were performed using Zwick ZHN, 2N instrument with a Berkovich nano indenter. Nano indentation modulus and nano indentation hardness of the material after welding was measured starting from the friction stir zone towards the base material along a line as described in figure 15. The red arrow represents the location and direction of the measurement points. The results revealed that the material nano indentation modulus and hardness increased from center of the weld towards the base material. Calleja et al. (1981) and Crist et al. (1989) reported that the modulus and hardness of polyethylene materials are proportional to crystallinity. It can be assumed that crystallinity has also increased from the center of the weld to the base material. Similarly, it was shown by Inaniwa et al. (2013) and Moreno et al. (2018) that hardness in the stir zone was lower than that in the base material by about 11%. One should consider here that micro voids and cavities might have affected the nano indentation test results to some extent, which may explain the scatter of the data given in Figure 15.

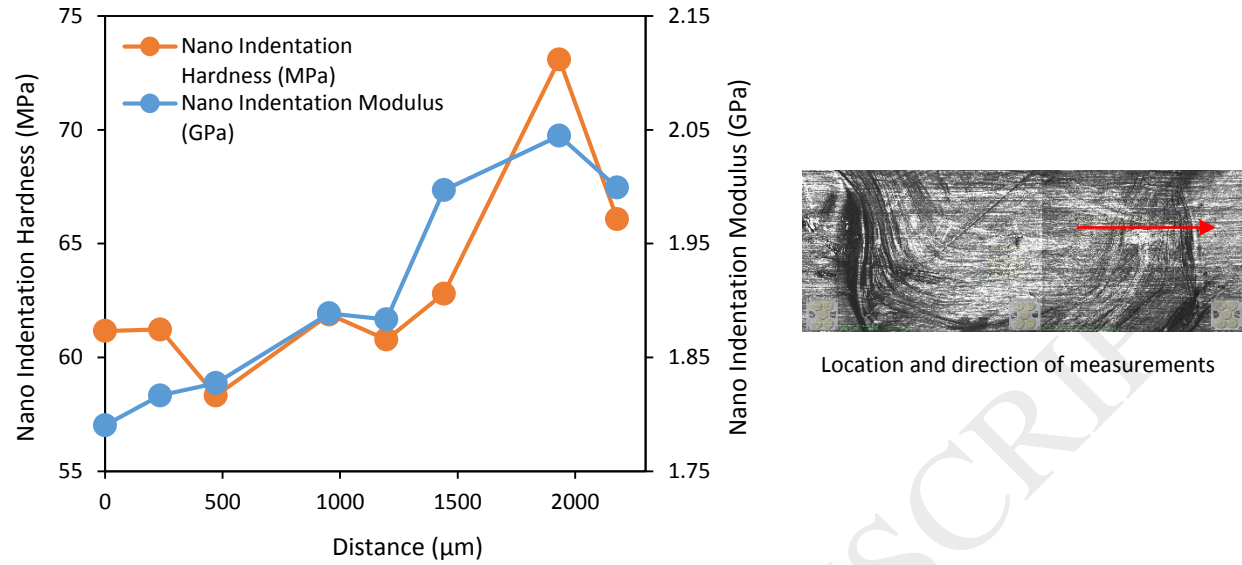


Figure 15. Nano indentation modulus and hardness of material along the red line given in figure 2.

3.8 Effect of process parameters

The effects of welding process parameters on welding temperatures, amount of defects, down force and tensile strength were examined by analysis of variance (ANOVA). The test whether or not an experimental parameter affects the outcome of the experiment is evaluated by the P-value, the calculated probability that the null hypothesis is true. The smaller the P-value, the smaller the probability that the results could be random (i.e. happened by chance). The significance level α is the threshold that the P-values are measured against and its value is associated with the confidence level of the results. For results with a 95% confidence level, the value of alpha is 0.05. The confidence level here means that if the experiment was repeated again and again the same results would be obtained 95% of the time. In view of this, a discussion of the statistically significant (most probable) correlations between experimental parameters and the results is given below. The relationships between process parameters and outcomes are also shown by the main effects plots in figure 16.

Factorial analysis of the maximum weld line temperature measured by the infrared camera on the top surface of the weld indicated that no statistically significant correlation existed between the process parameters and these temperatures (the P-values were much greater than 0.05 for all factors and their interactions). This is mainly due to melting of the material at the surface under the tool shoulder. During material melting, process generated heat is consumed in phase change and no significant temperature rise is observed. Therefore, the maximum surface temperatures remained in the range from 120 to 140 °C, regardless of the level of the experimental parameters. Figure 16(a) shows the effect of rotation speed on the under-weld peak temperature. Higher rotational speeds led to higher under-weld peak temperatures, which is believed to be due to the higher frictional heat input. The P-value for the rotation speed was 0.085, indicating that this parameter has an influence on the under-weld peak temperature (with a 91% confidence level). The effects of welding speed and penetration depth on the under-weld peak temperatures were statistically insignificant. The effects of parameters interactions were also non-significant.

Figure 16(b) shows the effect of the welding speed on the total area of weld defects appearing on the cross section of the weld (i.e. macro-voids, wormholes, and grooves). An increase in the welding speed generally led to an increase in the defects area due to abnormal mixing conditions. Also, at higher welding speeds the time for heat diffusion to the lower part of the thickness is less and the material temperatures are lower and its flow ability is less. This is consistent with observations in welding aluminum alloys (Nandan et al., 2008). The P-value of welding speed was 0.019, which is much less than $\alpha = 0.05$ used for a 95% confidence level. The effects of the rotation speed and penetration depth on total defects area were statistically insignificant. The

effects of parameters interactions were also non-significant. Figure 16(c) shows the effect of rotation speed on the down force. An increase in the rotation speed generally caused a decrease in the down force and the P-value for the rotation speed was 0.01. There is also some evidence that the down force is influenced by the depth of penetration, with a P-value of 0.059. The down force generally decreased with an increase in the penetration depth. Increasing both rotation speed and penetration depth increases the frictional energy input, causing the temperature to rise and the material to become softer and no longer able to support the tool shoulder, and thus causing the down force to drop. The effects of the welding speed and the parameters interactions on the down force were found to be statically insignificant. Figure 16(d) shows the effect of penetration depth of the yield strength of the weld. Factorial analysis of the yield strength indicated that the depth of penetration of the tool has the most significant influence with a P-value of 0.048, whereas the effects of welding speed and rotation speed were statistically insignificant. An increase in the penetration depth resulted in an increase in the average yield strength of the welded samples. Apparently, increasing the penetration depth causes an increase in the weld temperature, leading to better mixing and better bonding at the root of the weld. As discussed in sections 3.5, bonding at the root of the weld contributed significantly to the strength of the welded joint.

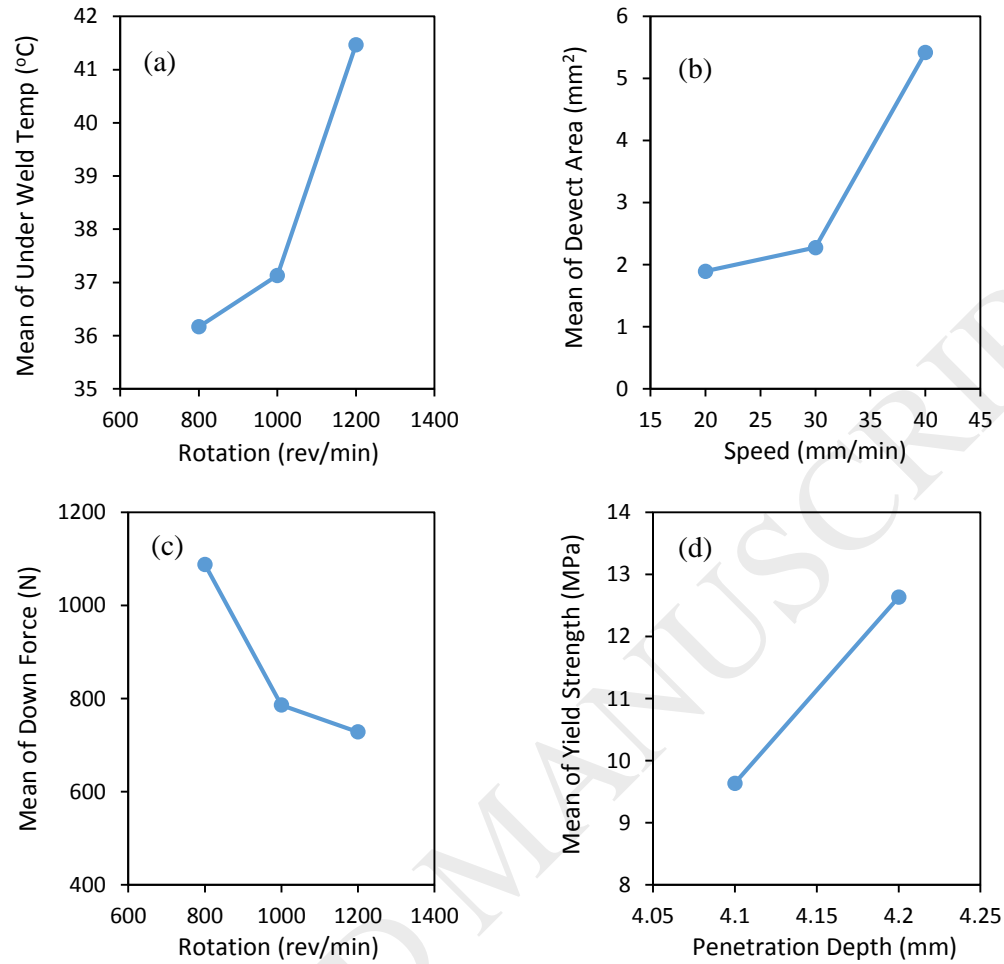


Figure 16. Main effect plots showing significant correlations between process parameters and responses, (a) under weld temperature, (b) total defect area, (c) down force and (d) tensile strength.

4 Conclusions

Friction stir welding of commercially available pipe-grade HDPE-carbon black composite was performed and the effects of pin rotational speed, welding speed and penetration depth on welding temperatures, down force and weld quality were investigated. Fracture surfaces of the welded samples were also analyzed. The major findings of this study are as follows:

- Defects were present in all welds to some extent and varied from micro-voids to large grooves and tunnels. The total defect area was influenced mainly by the welding speed.

- Numerical simulation of the heat conduction problem allowed the visualization of zones where melting has occurred under the rotating shoulder and at the trailing side of the rotating pin.
- The movement of molten material to the advancing side and its subsequent ejection resulted in the formation of large voids on this side.
- Crystallinity and hardness increased in the direction from the center of the weld to the base material due to higher temperatures under the tool shoulder.
- Fracture morphology of the welded joint exhibited mixed modes of fracture including ductile deformation, fibrillation and brittle fracture.
- Ductile deformation occurred in areas where good fusion took place due melting at the top region, proper mixing in the stir zone and forging at the root region.
- The tensile strength of the joint increased with increasing penetration depth due to higher process temperatures and improved bonding by hot forging at the root.

Acknowledgments

The authors would like to thank Borouge Innovation Center for providing the HDPE-CB material and the testing facility for conducting the tensile tests. The authors also thank Mr. Michael Heier of Zwick GmbH for performing the nano indentations tests, and Ms. Abeer Al Yafeai of the Chemical Engineering Department at Khalifa University for helping with the SEM imaging.

References

- Azarsa, E., Mostafapour, A. Experimental investigation on flexural behavior of friction stir welded high density polyethylene sheets. *Journal of Manufacturing Processes* Vol. 16 (2014): pp. 149–155.
- Bozkurt, Y. The optimization of friction stir welding process parameters to achieve maximum tensile strength in polyethylene sheets. *Materials and Design* Vol. 35 (2012): pp. 440–445.
- Calleja, F.J.B., Salazar, J.M., Čačković, H., Loboda-Čačković, J. Correlation of hardness and microstructure in unoriented lamellar polyethylene, *J. Mater. Sci.* 16 (1981) 739–751.
- Crist, B., Fisher, C.J., Howard, P.R. Mechanical properties of model polyethylenes: tensile elastic modulus and yield stress, *Macromolecules*. 22 (1989) 1709–1718.
doi:10.1021/ma00194a035.
- Deveci, S., Antony, N., Eryigit, B. Effect of carbon black distribution on the properties of polyethylene pipes part 1: Degradation of post yield mechanical properties and fracture surface analyses, *Polym. Degrad. Stab.* 148 (2018) 75–85. doi:10.1016/j.polymdegradstab.2018.01.011.
- Deveci, S., Oner, M. Effects of thermo-fatigue loading, hydrostatic pressure, and heat aging on the free-volume and crystalline structure of polypropylene-co-ethylene random copolymer pipes, *Polym. Eng. Sci.* 55 (2015) 641–650. doi:10.1002/pen.23930.
- dos Santos, W.N., de Sousa, J.A., Gregorio Jr., R. Thermal conductivity behaviour of polymers around glass transition and crystalline melting temperatures. *Polymer Testing* Volume 32, Issue 5, August 2013, Pages 987-994.
- Eslami, S., Ramos, T., Tavares, P.J., Moreira, P.M.G.P. Effect of friction stir welding parameters with newly developed tool for lap joint of dissimilar polymers. *Procedia Engineering* Vol. 114 (2015): pp. 199 – 207.

Fawaz, J., Deveci, S., Mittal, V. Molecular and morphological studies to understand slow crack growth (SCG) of polyethylene, *Colloid Polym. Sci.* 294 (2016) 1269–1280. doi:10.1007/s00396-016-3888-5.

Hoseinlghab, S., Mirjavadi, S.S., Sadeghian, N., Jalili, I., Azarbarmas, M., Givi, M.K. Influences of welding parameters on the quality and creep properties of friction stir welded polyethylene plates. *Materials and Design* Vol. 67 (2015): pp. 369–378.

Inaniwa, S., Kurabe, Y., Miyashita, Y., Hori, H. Application of friction stir welding for several plastic materials, *Proceedings of the 1st International Joint Symposium on Joining and Welding 2013*, Editor(s): Hidetoshi Fujii Pages 137-142

Kim, H-J, Kim, N-K, Kwak, J-S, Heat flux distribution model by sequential algorithm of inverse heat transfer for determining workpiece temperature in creep feed grinding. *Int. J. Mach Tool Manuf.* 46 (2006) 2086-2093.

Kiss, Z., Czigány, T. Microscopic analysis of the morphology of seams in friction stir welded polypropylene. *eXPRESS Polymer Letters* Vol.6, No.1 (2012) 54–62.

Mandelkern, L., Alamo, R.G. Thermodynamic quantities governing melting, in: *Phys. Prop. Polym. Handb.*, Springer, 2007: pp. 165–186.

Moreno-Moreno, M., Macea Romero, Y., Rodríguez Zambrano, H. et al. Mechanical and thermal properties of friction-stir welded joints of high density polyethylene using a non-rotational shoulder tool. *Int J Adv Manuf Technol* (2018) 97: 2489.

<https://doi.org/10.1007/s00170-018-2102-y>

Muñoz, S. Friction Stir Welding FSW of Gas Polyethylene Pipes. *Proceedings of the 6th Pan American Conference for NDT*. Cartagena, Colombia, 12-14 August 2015.

www.ndt.net/app.PANNDT2015.

Nandan, R., DebRoy, T., Bhadeshia, H.K.D.H. “Recent advances in friction stir welding – Process weldment structure and properties.” *Progress in Materials Science* Vol. 53 (2008): pp. 980–1023.

Pirizadeh, M., Azdast, T., Ahmadi, S.R., Shishavan, S.M., Bagheri, A. Friction stir welding of thermoplastics using a newly designed tool. *Materials and Design* Vol. 54 (2014): pp. 342–347.

Simões, F., Rodrigues, D.M. Material flow and thermo-mechanical conditions during Friction Stir Welding of polymers: Literature review, experimental results and empirical analysis. *Materials and Design* Vol. 59 (2014): pp. 344–351.

Squeo, Erica Anna, Bruno, Giuseppe, Guglielmotti, Alessandro, Quadrini, Fabrizio. Friction Stir Welding of Polyethylene Sheets. *The Annals of “DUNĂREA DE JOS” University of Galati Fascicle V, TECHNOLOGIES IN MACHINE BUILDING, ISSN 1221 – 4566* (2009): pp. 241-246.

Vijendra, B., Sharma, A. Induction heated tool assisted friction-stir welding (i-FSW): A novel hybrid process for joining of thermoplastics. *Journal of Manufacturing Processes* Vol. 20 (2015): pp. 234–244.

Whitelaw, Jim H. “CONVECTIVE HEAT TRANSFER,” <http://thermopedia.com/content/660/>, accessed 7/12/2018. DOI: 10.1615/AtoZ.c.convective_heat_transfer

Yan, Y., Shen, Y., Lan, B., Gao, J. Influences of friction stir welding parameters on morphology and tensile strength of high density polyethylene lap joints produced by double-pin tool. *Journal of Manufacturing Processes* Vol. 28 (2017): pp. 33–40.

Zafar, A., Awang, M., Khan, S., Emamian, S. Visual Analysis of Material Flow During Friction Stir Welding of Nylon-6. *ARPN Journal of Engineering and Applied Sciences*. VOL. 11, NO. 6, (2016): 4186-4190.